IET Quantum Communication

WILEY

The Institution of Engineering and Technology

ORIGINAL RESEARCH OPEN ACCESS

Cybersecure Synchronisation of Entangled Quantum Neural Networks With Reconfigurable Intelligent Surface and Quantum Key Distribution for 6G Holographic Communications

Raad S. Alhumaima[1,2] | Yassir Al-Karawi[2] | Hamed Al-Raweshidy[3]

[1]Department of Cyber Security Techniques, Imam Ja'afar Al-Sadiq University, Diyala, Iraq | [2]Department of Communications Engineering, University of Diyala, Diyala, Iraq | [3]College of Engineering, Design and Physical Sciences, Brunel University of London, Uxbridge, UK

Correspondence: Hamed Al-Raweshidy (hamed.al-raweshidy@brunel.ac.uk)

Received: 27 August 2025 | **Revised:** 4 March 2026 | **Accepted:** 24 March 2026

Keywords: quantum entanglement | quantum gates | quantum information | quantum mechanics | quantum theory | teleportation

ABSTRACT

This paper presents a cybersecure hybrid quantum–classical architecture for synchronising distributed quantum neural networks (QNNs) in 6G holographic communications. The proposed framework targets secure, low-latency and high-fidelity end-to-end operation under realistic noise and adversarial conditions. Multipartite Greenberger–Horne–Zeilinger (GHZ) entanglement supports gradient-consensus synchronisation, regularised by von Neumann entropy and trace distance. Holographic tensor teleportation is executed over reconfigurable intelligent surface (RIS)-assisted midhaul links protected by quantum key distribution (QKD). Joint optimisation of QNN parameters and RIS phases targets high end-to-end fidelity under noise. Qiskit simulations averaged over 100 trials achieve $F_{\text{avg}} = 0.961$, $E_{\text{sync}} = 0.010$ and $S(\rho) = 0.12$, with 22.5 ms end-to-end latency. Compared with reduced baselines without GHZ synchronisation or without RIS control, fidelity improves by 20%–28% and synchronisation divergence decreases by about 90%. Scalability, security stress scenarios, classical-feedback impairments, hyperparameter sensitivity and noisy intermediate-scale quantum (NISQ)-oriented error mitigation are all evaluated. The architecture scales gracefully to $N = 20$ distributed units with only 7% fidelity reduction, whereas mitigation improves fidelity by 7%–11% under moderate noise. Overall, the RIS-QKD-GHZ integration enables secure, low-latency and scalable quantum–classical 6G networking.

1 | Introduction

Sixth-generation (6G) networks aim to integrate quantum capabilities with classical communications and network-level cybersecurity. These infrastructures require architectures that deliver low-latency, high-fidelity and secure end-to-end operation under realistic noise and adversarial conditions [1–3]. In this context, distributed quantum neural networks (QNNs) at each distributed unit (DU) serve as both computation engines and entangled nodes. Their synchronisation and spatial topology significantly influence global performance and information integrity [4–6].

Recent studies have demonstrated the feasibility of qubit teleportation over midhaul links, whereas reconfigurable intelligent surfaces (RIS) enable programmable spatial control of wireless propagation [7, 8]. Recent surveys further underscore the transformative potential of RIS for smart wireless systems [9]. In parallel, variational quantum machine learning has shown promise for localised learning under entanglement and noise

[10]. However, prior work typically treats these capabilities in isolation. A unified network-oriented framework that jointly addresses entangled learning, holographic teleportation and RIS-assisted midhaul optimisation—whilst enforcing cybersecurity constraints—remains largely unexplored [11–13].

This paper proposes a *cybersecure quantum–classical network architecture* for synchronisation and control of entangled QNNs in 6G holographic communications. Each DU integrates a variational QNN, a teleportation engine for parameter/state exchange and an RIS module for adaptive phase control. Midhaul signalling is protected via quantum key distribution (QKD), providing information-theoretic keys for authenticated and confidential control/data channels. Multipartite Greenberger–Horne–Zeilinger (GHZ) entanglement maintains global parameter alignment across the network.

1.1 | Contributions

This paper makes four contributions:

1. A unified architecture that couples GHZ-based entangled QNN synchronisation with RIS-assisted midhaul control and QKD-secured orchestration.
2. A network-level formulation: QNN synchronisation as a distributed gradient-consensus problem regularised by von Neumann entropy and trace distance, jointly optimised with RIS phases to shape end-to-end fidelity.
3. A Qiskit-based evaluation under ideal and noisy conditions, including adversarial midhaul interference, with statistically consistent gains over reference baselines.
4. The experimental evaluation covers scalability ($N \in \{4, 8, 12, 16, 20\}$) under three GHZ-distribution topologies, security stress tests against six attacks and robustness to packet loss and jitter in classical feedback. Hyperparameter sensitivity via ablations and NISQ-oriented error mitigation are also assessed.

1.2 | Main Results

Across 100 runs, the proposed quantum neural holographic teleportation (QNHT) system attains average teleportation fidelity $F_{\text{avg}} = 0.961$, synchronisation error $E_{\text{sync}} = 0.010$, von Neumann entropy $S(\rho) = 0.12$ and end-to-end latency of 22.5 ms. Relative to baselines without GHZ synchronisation or without RIS control, fidelity improves by ≈20–28% and divergence (via E_{sync}) drops by ≈90%.

1.3 | Paper Organisation

Section 2 reviews related work. Section 3 presents the system architecture and quantum modelling. Section 4 formalises QNN synchronisation and RIS control. Section 5 details the simulation setup and parameters. Section 6 reports the comprehensive experimental evaluation, including scalability analysis, security stress tests, channel impairment effects, hyperparameter sensitivity and error mitigation techniques. Section 7 concludes and outlines future directions.

2 | Related Work

Research at the intersection of quantum learning, secure synchronisation and reconfigurable communications remains fragmented. Variational quantum neural networks (QNNs) for noisy intermediate-scale quantum (NISQ) devices [10, 14] are frequently examined as single-node circuits with minimal modelling of cross-node entanglement or distributed synchronisation. One representative direction investigates entangled-neuron circuits as nonlinear distributed quantum models, yet gradient consensus and phase-coherent alignment across nodes are left unaddressed, with communication assumed only at initialisation rather than maintained as a synchronisation process [15].

Within quantum communications, reports in *IET Quantum Communication* study free-space and satellite QKD largely as spatial/physical-layer optimisation under turbulence, pointing inaccuracies and geometric or polarisation losses. Wavefront control is typically realised by optical means—telescopes, beam steering or metasurfaces—in lieu of RIS-like adaptive surfaces [16–18]. To the best of current knowledge, there is no model in which time-varying wavefront control coevolves with quantum-learning-driven synchronisation (e.g., QNN alignment) and its impact on end-to-end teleportation fidelity is quantified. Work centred on teleportation in the same venue focuses on entanglement distribution and protocol design under idealised or block-fading regimes, with limited treatment of adversarial midhaul interference, evolving entanglement topologies or delayed classical feedback as explicit spatiotemporal elements [3, 19].

Quantum key distribution (QKD) is a cornerstone for information-theoretic keying in next-generation networks, enabling midhaul protection [20, 21]. Despite its well-established theoretical foundations, many deployments remain decoupled from quantum-learning workflows or are inserted as an isolated cryptographic layer. For instance, a QKD-assisted federated-learning design is proposed to strengthen aggregation privacy [20], yet entanglement-based synchronisation, tensorised state exchange for holographic coordination and RIS-steered channel control are not treated within a single networked formulation.

Scalability challenges in quantum networks have been addressed through various approaches. High-dimensional quantum teleportation protocols demonstrate improved channel capacity but face exponential resource scaling with increasing dimensions [22]. GHZ state distribution across multiple nodes exhibits fidelity degradation proportional to network size due to accumulated decoherence effects [23]. Security vulnerabilities in distributed quantum machine learning, including parameter poisoning and adversarial state manipulation, require detection mechanisms that may impact overall system throughput [24]. Recent advances in quantum cryptography

provide foundations for secure multiparty quantum protocols with composable security guarantees [25]. Error mitigation techniques, such as zero-noise extrapolation and probabilistic error cancelation, enable practical NISQ implementations with improved fidelity [26, 27]. Classical channel impairments, including packet loss and latency jitter, affect teleportation success rates. These impairments necessitate hybrid quantum–classical protocol designs that account for realistic network conditions.

This paper advances a unified network-oriented view: QNN synchronisation and RIS-assisted teleportation are aligned under a QKD-secured cybersecurity posture, tailored to quantum–classical 6G architectures. The model comprises:

- *Synchronisation layer*: global QNN parameter alignment via multipartite entanglement and gradient–consensus dynamics.
- *Teleportation layer*: RIS adaptation shapes propagation and enhances end-to-end fidelity under realistic noise.
- *Security layer*: QKD-based midhaul keying for confidentiality/integrity against eavesdropping and model-poisoning attacks.
- *Control/orchestration layer*: coordination of quantum–classical resources with performance and entropy monitoring.

The integrated view targets scalable, low-latency and quantum-secure operation over dynamic 6G infrastructures. A concise comparison is provided in Table 1 to position the present contribution.

3 | System Architecture and Modelling

The proposed system is modelled as a structured, partially observable hybrid quantum–classical network $\mathcal{G} = (\mathcal{V}, \mathcal{E})$. Each node $v_i \in \mathcal{V}$ denotes a distributed unit (DU) equipped with a quantum neural network (QNN), a holographic-teleportation module, and a reconfigurable intelligent surface (RIS). Edges $e_{ij} \in \mathcal{E}$ denote bidirectional midhaul connections secured via quantum key distribution (QKD) and dynamically reweighted by RIS phase responses. The overall system architecture is shown in Figure 1. As illustrated, the architecture comprises: (i) user equipment (UE) connected to distributed units (DUs) via RIS panels for enhanced signal propagation; (ii) edge cloud infrastructure hosting QNN processing with parameterised $R_Y(\theta)$ gates; (iii) QKD-protected midhaul links ensuring information-theoretic security and (iv) holographic links interconnecting quantum neural network layers for coordinated inference.

Each distributed unit i realises its QNN as a parameterised quantum circuit $\mathcal{U}_{\theta_i}$ of width n. The circuit operates on an input state prepared by amplitude encoding,

$$|\psi_i\rangle = \sum_{k=0}^{2^n-1} \alpha_k^{(i)} |k\rangle, \qquad \sum_{k=0}^{2^n-1} |\alpha_k^{(i)}|^2 = 1, \tag{1}$$

where $\{|k\rangle\}$ denotes the computational basis and the coefficients $\alpha_k^{(i)}$ are normalised amplitudes derived from local measurements [31].

The QNN consists of L layers, each composed of parameterised single-qubit R_Y rotations, Hadamard gates and entangling controlled-NOT (CNOT) operations:

$$\mathcal{U}_{\theta_i} = \prod_{\ell=1}^{L} \left[\prod_{q=1}^{n} R_Y(\theta_{i,\ell,q}) H_q \right] \cdot \prod_{q=1}^{n-1} \mathrm{CNOT}_{q,\, q+1}. \tag{2}$$

A representative layer of this structure is shown in Figure 2, where input qubits are initialised in the $|0\rangle$ state, processed by

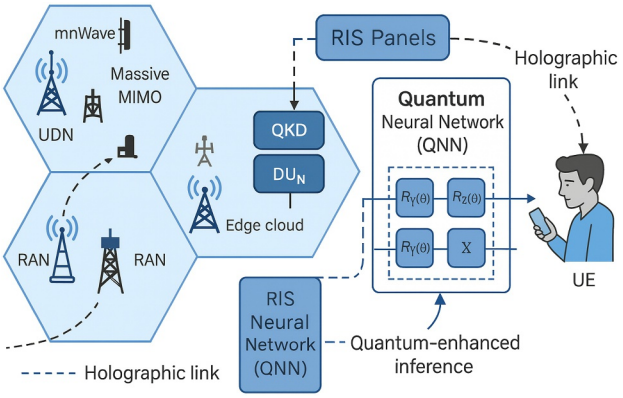

FIGURE 1 | Proposed hybrid quantum–classical network architecture integrating distributed QNNs, holographic teleportation modules, RIS and QKD-secured midhaul, with parameterised $R_Y(\theta)$ gates, QKD-protected midhaul links ensuring information-theoretic security and holographic links interconnecting quantum neural network layers. Key components include UE-to-DU connectivity via RIS panels, edge cloud QNN processing and QKD-protected links.

TABLE 1 | Comparison across QNN synchronisation, teleportation, RIS adaptation, QKD security, scalability analysis, and system-level modelling.

References	QNN sync	Teleportation	RIS adaptation	QKD security	Scalability	System modelling
[28]	✗	✓	✗	✗	✗	✗
[29]	✓	✗	✗	✗	✗	✗
[30]	✗	✓	✓	✗	✗	✗
[20]	✗	✗	✓	✓	✗	✗
[22]	✗	✓	✗	✗	✓	✗
This work	✓	✓	✓	✓	✓	✓

Hadamard gates, entangled via CNOT and finally rotated by $R_Y(\theta)$ gates [32].

Tables 2 and 3 provide an overview of the mathematical symbols and quantum gates used in the proposed QNN synchronisation and teleportation framework. Table 2 contains all the primary notations for quantum modelling and RIS control, whereas Table 3 contains all the gate operations used for encoding, entanglement and parameterised learning.

To ensure global synchronisation, ancilla qubits are entangled using a multipartite GHZ-like state:

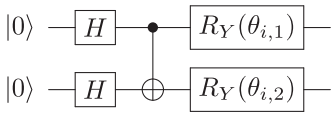

FIGURE 2 | Illustration of a single QNN layer at DU i with 2 qubits.

TABLE 2 | Key mathematical symbols used in the QNN synchronisation framework.

Symbol	Description
$\mathcal{U}_{\theta_i}$	Parameterised quantum neural network (QNN) circuit at DU i
θ_i	Trainable parameters (angles) of the QNN at DU i
$\|\mathcal{T}_i\rangle$	Holographically encoded tensor quantum state at DU i
ρ_i	Local mixed state at DU i, post-noise
F_{avg}	Average teleportation fidelity across all QNN links
$S(\rho)$	von Neumann entropy of quantum state ρ
E_{sync}	Synchronisation error between QNNs (gradient divergence)
D_{tr}	Trace distance between ideal and received quantum states
$\mathbf{\Phi}_i$	RIS phase-shift vector associated with DU i
ϕ	Optimised RIS phase (scalar tuning parameter)
p	Probability of depolarising noise in the quantum channel
$\mathcal{K}$	Kraus operator set modelling CPTP decoherence
t	Training epoch index
N	Number of distributed quantum nodes (DUs)
QBER	Quantum bit error rate for security monitoring
τ	Coherence lifetime for GHZ state fidelity decay
J	Maximum jitter amplitude (ms) in classical feedback channel
p_L	Packet loss probability in classical channel
η	Learning rate for QNN parameter updates
T	GHZ state refresh interval (synchronisation period)
λ_1, λ_2	Regularisation weights for entropy and trace distance

$$|\Psi\rangle_{1:N} = \frac{1}{\sqrt{2}}\left(|0\rangle^{\otimes N} + |1\rangle^{\otimes N}\right), \tag{3}$$

which maintains quantum correlations across N DUs and provides a reference for phase alignment.

The GHZ circuit is depicted in Figure 3, where Hadamard and CNOT gates entangle ancilla qubits across nodes.

The output quantum state from the QNN may undergo decoherence, modelled by a completely positive trace-preserving (CPTP) map:

$$\rho_i' = \sum_k K_k \rho_i K_k^\dagger, \quad \text{where} \sum_k K_k^\dagger K_k = I. \tag{4}$$

For example, depolarising noise is represented by $K_0 = \sqrt{1-p}I$ and $K_1 = \sqrt{p}X$ [33].

For quantum imaging and holographic inference tasks, each DU generates a quantum-encoded tensor state:

TABLE 3 | Quantum gate symbols used in the circuit.

Gate symbol	Gate description
H	Hadamard gate: Creates superposition
$R_Y(\theta)$	Y-rotation: Parameterised gate for QNN layers
$R_Z(\phi)$	Z-rotation: Phase encoding in QNN
	CNOT: Entanglement gate for QNN and GHZ
X^{m_2}	Pauli-X: Classical correction from Bell measurement
Z^{m_1}	Pauli-Z: Classical correction from Bell measurement
$U_3(\theta, \phi, \lambda)$	General SU(2) gate for universal QNN expressivity
V	Variational block: Multilayer quantum encoding
	Measurement: Standard in computational basis
GHZ	GHZ state preparation (Hadamard + CNOT chain)
Φ_i	RIS phase modulation gate for midhaul channel control
$\mathcal{E}$	Tensor encoder block: Maps $\|\psi\rangle \rightarrow \|?\rangle$

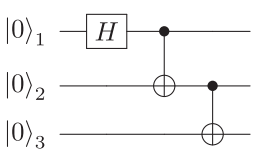

FIGURE 3 | Multipartite GHZ entanglement between DUs, enabling quantum synchronisation and state alignment for ρ_i.

$$|\mathcal{T}_i\rangle = \sum_{a,b,c} \gamma^{(i)}_{abc} |a\rangle|b\rangle|c\rangle, \tag{5}$$

which captures phase-sensitive quantum pixels in a three-dimensional lattice [34].

Teleportation proceeds via a joint Bell-basis measurement on the input qubit and the sender's share of a pre-shared Einstein–Podolsky–Rosen (EPR) pair. The resulting classical bits (m_1, m_2) are transmitted over a classical channel to the receiver, which applies conditional Pauli corrections to reconstruct the original quantum state:

$$\mathcal{U}_{\text{corr}} = X^{m_2} Z^{m_1}, \tag{6}$$

where X and Z are the standard Pauli operators. The teleportation process is illustrated in Figure 4.

3.1 | Tensor State Encoding and Decoding

The holographic tensor state $|\mathcal{T}_i\rangle$ encodes QNN parameters θ_i into quantum amplitudes suitable for teleportation. The encoding process maps the K-dimensional parameter vector to a d^3-dimensional Hilbert space via amplitude encoding:

$$\gamma^{(i)}_{abc} = \frac{\theta_{i,k}}{|\theta_i|_2}, \quad k = a \cdot d^2 + b \cdot d + c, \tag{7}$$

where the indices $(a, b, c) \in \{0, ..., d-1\}^3$ correspond to the three-qudit registers and d denotes the local Hilbert-space dimension per register. The encoding circuit prepares $|\mathcal{T}_i\rangle$ using a sequence of controlled rotations:

$$\mathcal{E} = \prod_{k=0}^{d^3-1} CR_Y\big(2 \arcsin(\gamma_k)\big) \cdot H^{\otimes 3n_q}, \tag{8}$$

where $n_q = \lceil \log_2 d \rceil$ qubits encode each register.

The decoded parameters satisfy $|\widehat{\theta}_j - \theta_i| \le \epsilon$ with high probability under standard fidelity–distance bounds (e.g., relating state infidelity to trace-distance deviation) [35], and the resulting reconstruction accuracy is empirically verified in the reported fidelity regimes.

The RIS propagation is modelled by a diagonal phase-shift matrix:

$$\mathbf{\Phi}_i = \text{diag}\big(e^{j\phi_{i,1}}, e^{j\phi_{i,2}}, ..., e^{j\phi_{i,M}}\big), \tag{9}$$

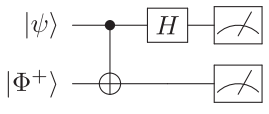

FIGURE 4 | Bell-state teleportation circuit used to transmit $|\psi\rangle$ across distributed QNNs.

where $\phi_{i,m}$ denotes the controllable phase shift applied by element m of RIS i and M is the total number of reflecting elements per RIS panel. This results in an effective quantum midhaul channel modelled as follows:

$$\mathbf{H}^{\text{eff}}_{ij} = \mathbf{H}^{(i)}_{\text{DU-RIS}} \mathbf{\Phi}_i \mathbf{H}^{(j)}_{\text{RIS-DU}} + \mathbf{H}^{(i,j)}_{\text{QKD}}, \tag{10}$$

where $\mathbf{H}^{(i,j)}_{\text{QKD}}$ captures the QKD-assisted protected link [20, 30].

To ensure coherent parameter updates and secure entanglement, the global synchronisation objective is formulated as a Lagrangian:

$$\begin{aligned}\mathcal{L}_{\text{sync}} = &\sum_{i \neq j} \big\| \nabla_{\theta_i} J_i - \nabla_{\theta_j} J_j \big\|^2 \\ &+ \lambda_1 \sum_i S(\rho_i) + \lambda_2 \sum_{i \neq j} D_{\text{tr}}\big(\rho_i, \rho_j\big),\end{aligned} \tag{11}$$

where $S(\rho_i) = -\text{Tr}(\rho_i \log \rho_i)$ is the von Neumann entropy reflecting the uncertainty of the local QNN state ρ_i and $D_{\text{tr}}(\rho_i, \rho_j) = \frac{1}{2}\text{Tr}\big|\rho_i - \rho_j\big|$ quantifies the distinguishability between entangled nodes [36].

The term $\nabla_{\theta_i} S(\rho_i)$ is given by:

$$\nabla_{\theta_i} S(\rho_i) = -\text{Tr}\big[(\log \rho_i + \mathbb{I}) \cdot \nabla_{\theta_i} \rho_i\big], \tag{12}$$

where gradients are computed via the parameter-shift rule [37].

The trace distance is defined as follows:

$$D_{\text{tr}}(\rho_i, \rho_j) = \frac{1}{2}\big\|\rho_i - \rho_j\big\|_1 = \frac{1}{2}\text{Tr}\Big[\sqrt{(\rho_i - \rho_j)^2}\Big], \tag{13}$$

Based on the trace distance in Equation (13), its gradient is approximated as follows:

$$\nabla_{\theta_i} D_{\text{tr}}(\rho_i, \rho_j) \approx \frac{1}{2} \sum_k \nabla_{\theta_i} \lambda_k, \tag{14}$$

where λ_k are the eigenvalues of $(\rho_i - \rho_j)^2$ [38].

All evaluations are performed using Qiskit's `quantum_info` module, and parameter gradients (including the trace-distance gradient in Equation (14)) are obtained via hybrid finite-difference and parameter-shift techniques.

The variational circuit structure shown in Figure 5 generates the local quantum state ρ_i. The parameters are updated via:

$$\begin{aligned}\theta_i^{(t+1)} = \theta_i^{(t)} - \eta\big(&\nabla_{\theta_i} J_i \\ &+ \lambda_1 \nabla_{\theta_i} S(\rho_i) + \lambda_2 \nabla_{\theta_i} D_{\text{tr}}(\rho_i, \rho_j)\big),\end{aligned} \tag{15}$$

where η is the learning rate.

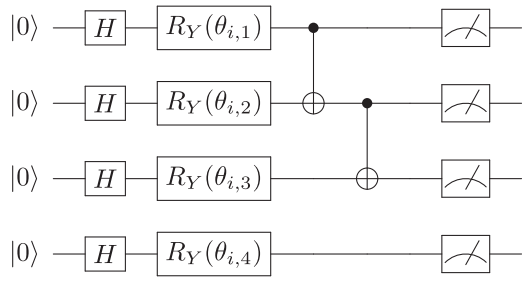

FIGURE 5 | Variational QNN circuit used to generate the output quantum state ρ_i at DU i.

4 | Quantum Neural Synchronisation and Teleportation Framework

To enable distributed quantum learning and state teleportation over 6G holographic networks, each distributed unit (DU) is equipped with a local quantum neural network (QNN), modelled as a parameterised variational quantum circuit (VQC) with trainable parameters θ_i. Input vectors are encoded using amplitude encoding [39]:

$$|\psi_{\text{in}}^{(i)}\rangle = \sum_{k=0}^{2^n-1} \alpha_k^{(i)} |k\rangle, \quad \text{where} \quad \sum_k |\alpha_k^{(i)}|^2 = 1. \tag{16}$$

4.1 | GHZ-Based Quantum Synchronisation

To ensure coherence and learning consensus across the distributed system, all DUs share a multipartite GHZ entangled state [39], following the amplitude encoding in Equation (16):

$$|\Psi\rangle_{1:N} = \frac{1}{\sqrt{2}}\left(|0\rangle^{\otimes N} + |1\rangle^{\otimes N}\right), \tag{17}$$

which serves as a quantum reference during synchronised QNN updates.

The circuit in Figure 6 integrates both the GHZ preparation and teleportation control flow, with classical corrections dynamically applied based on measurements.

The QNNs are synchronised by minimising the following loss [37]:

$$\begin{aligned}\mathcal{L}_{\text{sync}} = &\sum_{i\neq j} \left\| \nabla_{\theta_i} J_i - \nabla_{\theta_j} J_j \right\|^2 \\ &+ \lambda_1 \sum_i S(\rho_i) + \lambda_2 \sum_{i\neq j} D_{\text{tr}}(\rho_i, \rho_j),\end{aligned} \tag{18}$$

where $D_{\text{tr}}(\rho_i, \rho_j)$ is the trace distance between the reduced density matrices of DUs i and j.

To operationalise the above objective in a networked setting, a periodic, GHZ-assisted consensus routine is implemented that alternates between local VQC training and global parameter alignment. Algorithm 1 details this quantum neural synchronisation (QNS) procedure: each DU performs local forward passes and gradient computation, and every T rounds a shared GHZ state (Figure 6) anchors the synchronisation step, enabling authenticated gradient exchange and consistent parameter updates across the distributed system. The parameter update rule in Algorithm 1 implements the gradient-consensus component of the update rule in Equation (15), whereas the GHZ state preparation follows Equation (17).

ALGORITHM 1 | Quantum neural synchronisation (QNS).

Input : Initial QNN parameters $\{\boldsymbol{\theta}_i^{(0)}\}_{i=1}^N$, synchronisation interval T, learning rate η

Output: Aligned QNN parameters across N distributed units

for $t = 1, 2, \ldots$ **do** // global rounds
  for *each DU* i **do in parallel** // local DU updates
    Encode input state $|\psi_{\text{in}}^{(i)}\rangle$ via amplitude encoding
    Apply QNN circuit: $|\psi_{\text{out}}^{(i)}\rangle \leftarrow \mathcal{U}_{\boldsymbol{\theta}_i^{(t)}} |\psi_{\text{in}}^{(i)}\rangle$
    Compute local loss $J_i^{(t)}$ and gradient $\nabla_{\boldsymbol{\theta}_i} J_i^{(t)}$
  if $t \bmod T = 0$ **then** // synchronisation step
    Establish a shared GHZ state as in Fig. 6
    for *each DU pair* (i, j) **do** // pairwise exchange
      Exchange gradients $\nabla_{\boldsymbol{\theta}_i} J_i^{(t)}$ and $\nabla_{\boldsymbol{\theta}_j} J_j^{(t)}$
      Update parameters at DU i:

$$\boldsymbol{\theta}_i^{(t+1)} \leftarrow \boldsymbol{\theta}_i^{(t)} - \eta \left(\nabla_{\boldsymbol{\theta}_i} J_i^{(t)} - \nabla_{\boldsymbol{\theta}_j} J_j^{(t)} \right)$$

4.2 | Teleportation of Quantum Tensor States

Each QNN produces a quantum tensor state $|\mathcal{T}_i\rangle \in \mathbb{C}^{d\times d\times d}$, representing holographic information:

$$|\mathcal{T}_i\rangle = \sum_{a,b,c} \gamma_{abc}^{(i)} |a\rangle|b\rangle|c\rangle. \tag{19}$$

Teleportation of $|\mathcal{T}_i\rangle$ is achieved via a Bell-state measurement on the QNN output and a shared entangled ancilla [22]. Based on the classical outcome $m = (m_1, m_2)$, Pauli gates Z^{m_1} and X^{m_2} are applied to reconstruct the state.

For reproducibility and to explicitly capture the hybrid quantum–classical handshake, Algorithm 2 summarises the holographic teleportation protocol (HTP) used in our framework: the sender performs a Bell-basis measurement, the authenticated classical channel carries the two-bit outcome (m_1, m_2) and the receiver applies the conditional correction $\mathcal{U}_{\text{corr}} = X^{m_2} Z^{m_1}$ to reconstruct the transmitted tensor payload at DU j. The correction operation in Algorithm 2 implements Equation (6), whereas the tensor state encoding follows Equation (5).

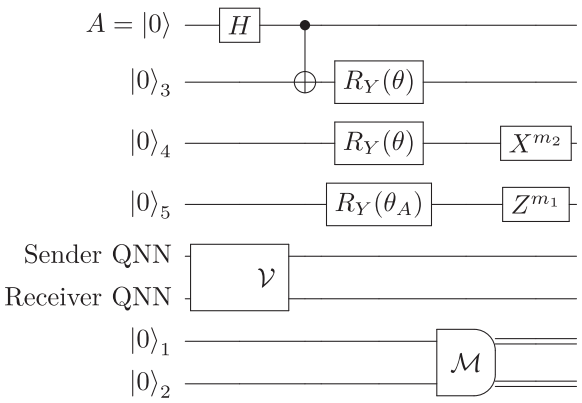

FIGURE 6 | Integrated QNN synchronisation and holographic teleportation circuit using `Qcircuit`. The GHZ entangler prepares control qubit A to synchronise QNN layers. Classical measurement outcomes (m_1 and m_2) guide Pauli corrections Z^{m_1} and X^{m_2}, ensuring successful tensor teleportation. The $R_Y(\theta)$ gates represent QNN parameterised rotations.

ALGORITHM 2 | Holographic teleportation protocol (HTP).

Input : Sender tensor state $|\mathcal{T}_i\rangle$ (Eq. 5) at DU i, shared Bell pair $|\Phi^+\rangle$ with receiver DU j
Output: Teleported tensor state $|\mathcal{T}_i\rangle$ reconstructed at DU j

for *teleportation session* **do in parallel**
  `// sender-side operations at DU` i
  Apply joint Bell measurement on $(|\mathcal{T}_i\rangle, |\Phi^+\rangle)$
  Obtain classical bits $m_1, m_2 \in \{0, 1\}$
for *classical channel* **do in parallel**
  `// authenticated classical feedback`
  Transmit (m_1, m_2) to DU j over the authenticated classical channel
for *receiver processing* **do in parallel**
  `// receiver-side correction at DU` j
  Apply the conditional correction:

$$\mathcal{U}_{\text{corr}} \leftarrow X^{m_2} Z^{m_1}$$

  Output the reconstructed state at DU j

4.3 | Joint Learning and Optimisation

Figure 7 provides a comprehensive outline of the joint optimisation loop (JOL), where the quantum neural network (QNN) updates, the RIS phase adaptation and the entanglement preservation all aim to optimise the fidelity and synchronisation in the distributed 6G system in coordination.

The training process is an iterative loop that encompasses the QNS procedure and the holographic teleportation protocol (HTP), in which both QNN parameters θ_i and RIS phase vectors $\phi_{i,m}$ are optimised together. The primary optimisation objective is the average teleportation fidelity, defined as follows:

$$F_{\text{avg}} = \mathbb{E}_{i,j}\left[\langle \mathcal{T}_i | \rho_j^{\text{recv}} | \mathcal{T}_i \rangle\right], \tag{20}$$

where $|\mathcal{T}_i\rangle$ represents the transmitted quantum tensor state and ρ_j^{recv} is the received density matrix at DU j [36].

The fidelity is highly sensitive to the effective quantum channel H_{ij}^{eff}, which is dynamically modulated by the RIS phase-shift matrix Φ_i as follows:

$$\mathbf{H}_{ij}^{\text{eff}} = \mathbf{H}_{\text{DU-RIS}}^{(i)} \boldsymbol{\Phi}_i \mathbf{H}_{\text{RIS-DU}}^{(j)} + H_{\text{QKD}}^{(i,j)}. \tag{21}$$

Thus, the optimisation of $\phi_{i,m}$ becomes a key control task that directly impacts teleportation quality and QNN synchronisation [30].

In parallel, the QNN parameters are updated by minimising the global synchronisation loss function:

$$\begin{aligned}\mathcal{L}_{\text{sync}} = &\sum_{i \neq j} \left\| \nabla_{\theta_i} J_i - \nabla_{\theta_j} J_j \right\|^2 \\ &+ \lambda_1 \sum_i S(\rho_i) + \lambda_2 \sum_{i \neq j} D_{\text{tr}}\left(\rho_i, \rho_j\right),\end{aligned} \tag{22}$$

where $S(\rho)$ is the von Neumann entropy and D_{tr} is the trace distance between quantum states, as defined earlier [36].

The loop also incorporates periodic refreshment of the multipartite GHZ entangled state, which is used as a reference for QNN alignment. Due to inevitable decoherence in quantum channels, the GHZ state fidelity degrades over time:

$$F_{\text{GHZ}}(t) \approx \exp(-t/\tau), \tag{23}$$

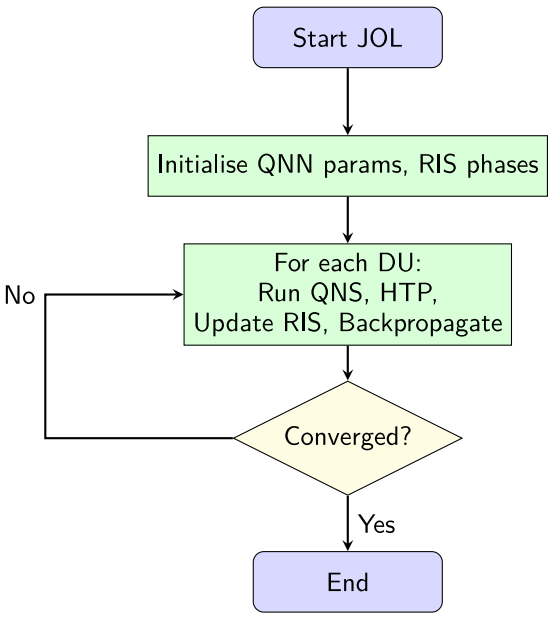

FIGURE 7 | Flowchart of the joint optimisation loop (JOL), integrating QNN synchronisation (QNS), holographic teleportation (HTP), RIS phase tuning and GHZ entanglement refresh.

where τ denotes the coherence lifetime. To maintain entanglement integrity, the GHZ state is refreshed every T rounds, ensuring the synchronisation reference remains valid throughout training [40].

Algorithm 3 formalises the JOL that coordinates the end-to-end operation of the proposed framework. The loop repeatedly executes QNS (Algorithm 1) and HTP (Algorithm 2) at each DU, refines RIS phases via a fidelity-driven maximisation step and refreshes GHZ entanglement every T rounds to mitigate entanglement drift. This formulation makes the timing of quantum exchanges and authenticated classical feedback explicit and is consistent with the flow in Figure 7. The RIS optimisation in Algorithm 3 maximises the fidelity objective in Equation (20), whereas the QNN parameters are updated according to Equation (15), driven by the synchronisation loss $\mathcal{L}_{\text{sync}}$ defined in Equation (11).

ALGORITHM 3 | Joint optimisation loop (JOL).

Input : Initial QNN parameters $\{\boldsymbol{\theta}_i^{(0)}\}_{i=1}^{N}$, RIS phases $\{\phi_{i,m}^{(0)}\}$, tensor-encoded inputs, learning rate η, GHZ refresh period T
Output: Converged $\{\boldsymbol{\theta}_i\}$, $\{\phi_{i,m}\}$, and average fidelity F_{avg}

while *not converged* **do** // outer loop until convergence
  for *each DU* i **do** // iterate over distributed units
    Run QNS (Algorithm 1)
    Execute teleportation via HTP (Algorithm 2)
    Update RIS phases:

$$\phi_{i,m}^{(t+1)} \leftarrow \arg\max_{\phi} \; F_{\text{avg}}^{(i)}(\phi)$$

    Update QNN parameters:

$$\boldsymbol{\theta}_i^{(t+1)} \leftarrow \boldsymbol{\theta}_i^{(t)} - \eta \nabla_{\boldsymbol{\theta}_i} \mathcal{L}_{\text{sync}}$$

  if $t \bmod T = 0$ **then** // periodic entanglement maintenance
    Refresh GHZ entanglement state across all DUs
  $t \leftarrow t + 1$

5 | Simulation and Evaluation Setup

To evaluate the proposed framework of quantum neural synchronisation and holographic teleportation for distributed 6G applications, a full simulation stack is constructed using IBM Qiskit with tensor modelling in NumPy. The testbed instantiates $N = 4$ distributed units (DUs), each comprising a variational quantum neural network (QNN), a holographic tensor encoder and an RIS for midhaul control. Each QNN is realised as a 4-qubit VQC with parameterised R_Y and R_Z rotations and entangling CNOT gates. The evaluation considers $N \in \{4, 8, 12, 16, 20\}$ distributed units to characterise scalability under increasing system scale. For each N, three GHZ-distribution/network layouts (star, mesh and two-level hierarchical) are evaluated as defined in Section 6, whilst keeping the per-node QNN depth/width and RIS configuration identical. All scalability results are averaged over 100 independent trials per configuration to ensure statistical robustness across network sizes.

After normalising the classical features, they are embedded in a quantum Hilbert space via amplitude encoding:

$$|\psi_{\text{in}}^{(i)}\rangle = \sum_{k=0}^{2^n-1} \alpha_k^{(i)} |k\rangle, \quad \text{with} \quad \sum_k |\alpha_k^{(i)}|^2 = 1.$$

Neural synchronisation between DUs is maintained using a multipartite GHZ-like entangled ancilla state that is refreshed periodically every $T = 20$ iterations to reduce the effects of decoherence. The gradient updates follow the same parameter-shift rule as before. Additionally, to build resilience against possible adversarial interference through midhaul links, all synchronisation operations are conducted over QKD authenticated entanglement links that are monitored for entropy and trace distance.

RIS modules are abstracted as 4×4 unitary phase matrices $\boldsymbol{\Phi}_i$ dynamically optimised at each synchronisation round. The teleportation encoder maps the output state $|\psi_i\rangle$ into a tensorial quantum payload $|\mathcal{T}_i\rangle \in \mathbb{C}^{d\times d\times d}$ using a custom quantum tensor grid extension:

$$|\mathcal{T}_i\rangle = \sum_{a,b,c} \gamma_{abc}^{(i)} |a\rangle|b\rangle|c\rangle, \quad \text{with} \quad \gamma_{abc}^{(i)} \in \mathbb{C}.$$

Two teleportation modes are considered. The first is an ideal Bell-state teleportation mode with perfect entanglement and noiseless operations. The second is a noise-injected mode that simulates teleportation through depolarising channels acting on the midhaul link. The depolarising process is modelled with Kraus operators $\{K_0, K_1, K_2, K_3\}$, where for error rate p, $K_0 = \sqrt{1-p}\, I$, $K_1 = \sqrt{p/3}\, X$, $K_2 = \sqrt{p/3}\, Y$ and $K_3 = \sqrt{p/3}\, Z$. At the receiver, the conditional Pauli correction from $\{I, X, Z, XZ\}$ is applied according to the two classical bits produced by the Bell measurement.

The evaluation metrics are defined as follows:

- *Average Fidelity* (F_{avg})—The overlap between the tensor representations of the states sent and received.
- *Trace Distance* (D_{tr})—The distance between the reduced density matrices of the sent and received states post-teleportation.
- *Synchronisation Error* (E_{sync})—The L_2 norm of the divergence of the QNN gradients across DUs.
- *Teleportation Latency*—The time required for end-to-end delay from QNN encoding to decoding post-teleportation.

- *Quantum Bit Error Rate (QBER)*—The ratio of erroneous bits to total bits in QKD key generation, used for security monitoring with threshold QBER < 0.11 for BB84 protocol [41, 42].

All quantum circuits are compiled using Qiskit's transpiler at optimisation level 2 to reduce circuit depth and gate errors.

The noisy simulation used the `FakeAthens` and `FakeJakarta` backends to replicate realistic device behaviour.

Beyond depolarising noise, the proposed workflow is additionally validated under physically motivated channel errors to better reflect midhaul/hardware impairments. Specifically, (i) amplitude damping with Kraus operators $E_0 = \begin{bmatrix} 1 & 0 \\ 0 & \sqrt{1-\gamma} \end{bmatrix}$ and $E_1 = \begin{bmatrix} 0 & \sqrt{\gamma} \\ 0 & 0 \end{bmatrix}$ (energy relaxation) and (ii) phase damping (dephasing) with $E_0 = \sqrt{1-\lambda}\, I$, $E_1 = \sqrt{\lambda}\,|0\rangle\langle 0|$ and $E_2 = \sqrt{\lambda}\,|1\rangle\langle 1|$ are tested, where γ and λ capture relaxation and dephasing strengths, respectively.

Classical-channel impairments are modelled explicitly for the Bell-outcome feedback path: packet loss is injected as an i.i.d. Bernoulli process with loss probability p_L per message, and latency jitter is modelled as an additive bounded random delay with maximum amplitude J ms applied to the feedback packets. Retransmissions are triggered upon timeout, and the corresponding retransmission/timeout rates are reported in Section 5 and Tables 4 and 5. The impairment parameters ($p_L \leq 5\%$ and $J \leq 10$ ms) are consistent with 5G NR and anticipated 6G ultrareliable low-latency communication (URLLC) specifications. Future implementations could leverage transmission control protocol (TCP) for reliable delivery or user datagram protocol (UDP) with application-layer automatic repeat request (ARQ) for latency-sensitive quantum feedback.

TABLE 4 | Impact of classical channel packet loss on fidelity.

Packet loss (%)	F_{avg}	E_{sync}	Retrans. (%)
0	0.961	0.010	0
1	0.942	0.014	1.5
5	0.876	0.028	8.2
10	0.782	0.051	18.7
20	0.651	0.089	42.3

Note: Each row reports the mean over 100 trials at the given packet-loss rate and standard deviations remain below 0.025 for F_{avg}.

TABLE 5 | Impact of classical channel jitter on system performance.

Jitter (ms)	F_{avg}	E_{sync}	Timeout (%)
0	0.961	0.010	0
2	0.952	0.012	0.5
5	0.938	0.015	2.1
10	0.915	0.022	5.8
20	0.878	0.035	14.2

Note: Each row reports the mean over 100 trials at the given jitter level and standard deviations remain below 0.02 for F_{avg}.

The end-to-end simulation workflow and evaluation pipeline are illustrated in Figure 8, highlighting the DU-side QNN execution, GHZ-based synchronisation, RIS-steered quantum channel effects and the authenticated classical-feedback path used for Bell-outcome corrections. As shown, each DU encodes classical features into quantum states via amplitude initialisation, applies parameterised $R_Y(\theta)$ rotations and generates tensor states $|\mathcal{T}_i\rangle$ for teleportation. The RIS phase modulation Φ_i controls midhaul propagation, whilst QKD ensures security.

6 | Results and Analysis

This section provides a comprehensive performance assessment of the proposed QNHT architecture. The evaluation encompasses baseline performance metrics, scalability across network sizes, noise resilience and sensitivity analysis, security robustness against adversarial attacks, channel impairment analysis, hyperparameter sensitivity and comparative evaluation against baselines.

6.1 | Baseline Performance Evaluation

The architecture is first evaluated under the baseline configuration of $N = 4$ DUs with 4-qubit QNNs, using four primary measures: teleportation fidelity, synchronisation error, quantum entropy and Bloch-vector distortion.

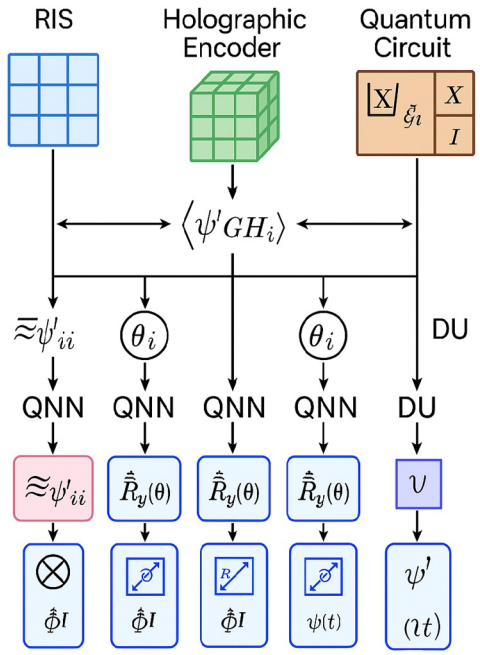

FIGURE 8 | Simulation and evaluation setup: DU-side QNN execution with amplitude encoding, GHZ-based synchronisation, RIS-steered quantum channels and QKD-mediated security. Fidelity and trace distance are evaluated at the receiver.

Figure 9 shows that the average quantum fidelity F_{avg} decreases as a function of the depolarising-noise probability p (see Equation 24).

$$K_0 = \sqrt{1-p}\, I, \quad K_1 = \sqrt{p/3}\, X, \\ K_2 = \sqrt{p/3}\, Y, \quad K_3 = \sqrt{p/3}\, Z. \tag{24}$$

Across $p \in [0, 0.15]$, F_{avg} remains above 0.85, indicating resilience to moderate levels of decoherence.

Figure 10 reports the synchronisation error E_{sync} computed as the L_2 norm of gradient divergence across QNNs. The error decreases logarithmically across epochs due to the gradient-aligned update rule in Equation (15) and Algorithm 1.

In parallel, Figure 11 shows the reduction in von Neumann entropy $S(\rho)$ as synchronisation proceeds, indicating an increase in the purity and coherence of local quantum states ρ_i.

Latency due to quantum teleportation is shown in Figure 12. The noisy case introduces additional latency due to error mitigation and conditional unitary correction.

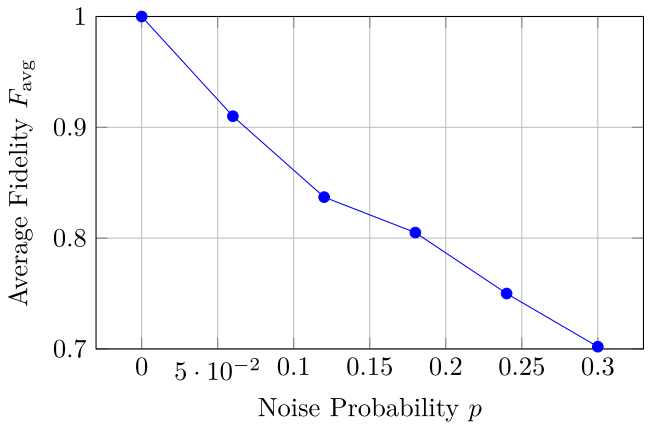

FIGURE 9 | Effect of depolarising noise on teleportation fidelity F_{avg}, evaluated over $p \in [0, 0.30]$ using the Kraus operator model. Fidelity remains above 0.85 for $p \leq 0.15$, confirming resilience to moderate decoherence in the QNHT framework.

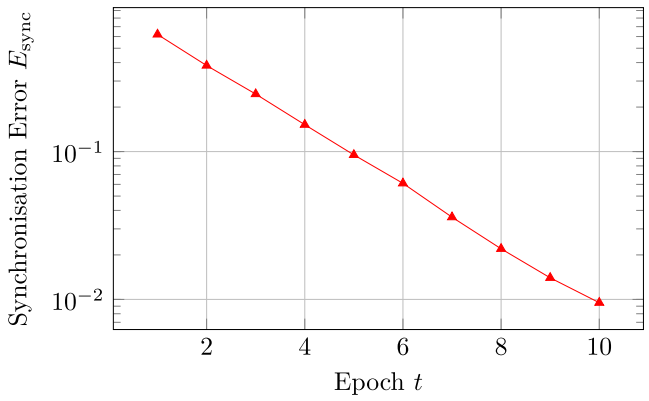

FIGURE 10 | Convergence of QNN synchronisation error E_{sync} across training epochs for $N = 4$ DUs, averaged over 100 independent trials.

A geometric representation of Bloch-vector distortion due to decoherence is presented in Figure 13. This distortion indicates a loss of precision in reconstructing the tensor state $|\mathcal{T}_i\rangle$ during teleportation. The visualisation demonstrates how phase noise causes state vectors to deviate from their ideal positions on the

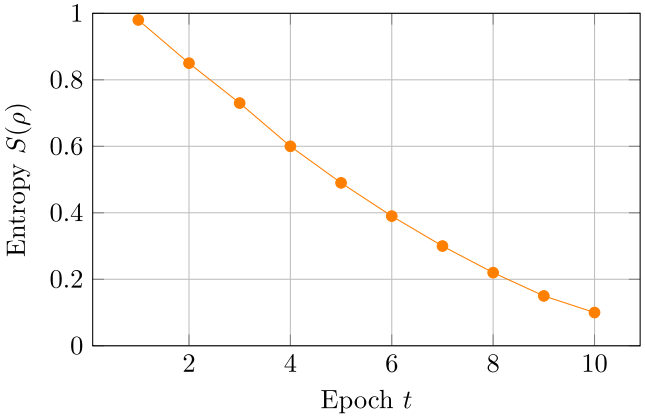

FIGURE 11 | Reduction of von Neumann entropy $S(\rho)$ during QNN synchronisation for $N = 4$ DUs, averaged over 100 trials. Lower entropy indicates increased state purity and coherence.

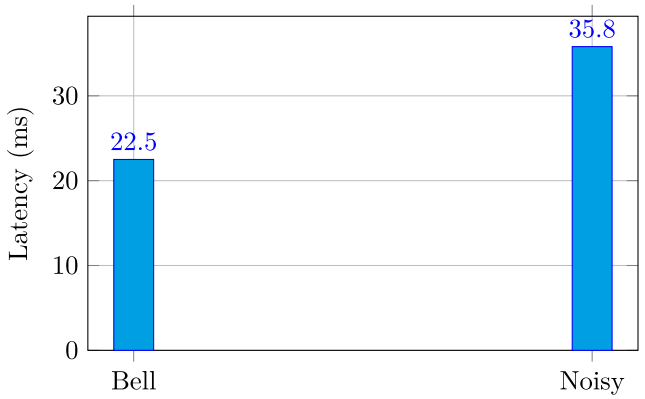

FIGURE 12 | Teleportation latency (ms) under ideal Bell-state and noise-injected ($p = 0.05$) scenarios for $N = 4$ DUs. The additional latency in the noisy case arises from error mitigation overhead.

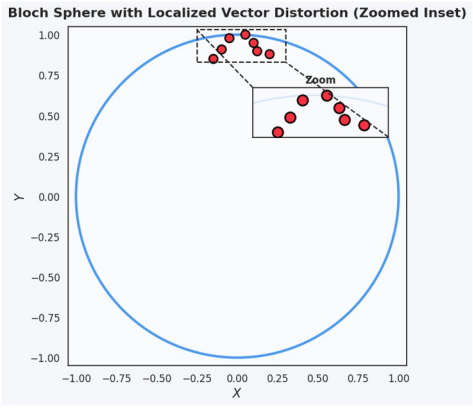

FIGURE 13 | Bloch vector distortion in the XY plane due to phase noise, showing ideal states (blue) and noise-affected states (red). The zoomed inset highlights the localised distortion region.

Bloch sphere, with larger deviations corresponding to increased decoherence.

6.2 | Scalability Analysis

To evaluate scalability beyond the baseline configuration, the number of distributed units is systematically increased to $N \in \{4, 8, 12, 16, 20\}$ whilst maintaining identical QNN architectures and RIS configurations per node.

6.3 | Performance Versus Network Size

Table 6 summarises the key metrics as a function of network size. The results demonstrate graceful degradation: average fidelity decreases from $F_{\text{avg}} = 0.961$ at $N = 4$ to $F_{\text{avg}} = 0.893$ at $N = 20$, representing only a 7.1% reduction despite a 5× increase in network complexity.

6.4 | Network Topology Comparison

Three network topologies for GHZ distribution are compared: (1) Star topology where a central hub distributes entanglement to all DUs, (2) mesh topology with all-to-all entanglement links and (3) hierarchical topology using a two-level tree with intermediate aggregation nodes. Table 7 presents the comparison at $N = 12$ DUs.

Figure 14 illustrates the scalability advantage of QNHT over the unsynchronised baseline. The gap widens with increasing N, demonstrating that GHZ-based synchronisation becomes increasingly critical for larger networks.

6.5 | Resource and Bandwidth Scaling

Practical scalability is determined not only by fidelity and convergence behaviour but also by the physical resources required to distribute multipartite entanglement and to exchange encrypted classical control messages. Accordingly, the growth of entanglement-link count and control-plane overhead with the number of distributed units N is quantified under the three considered GHZ-distribution topologies.

Let $L(N)$ denote the number of quantum entanglement links required to support GHZ delivery or equivalent entanglement-assisted coordination among N DUs. For the star, mesh and a two-level hierarchical topology with C aggregation groups, the link scaling can be summarised as follows:

$$L_{\text{star}}(N) = N - 1,$$
$$L_{\text{mesh}}(N) = \frac{N(N-1)}{2}, \tag{25}$$
$$L_{\text{hier}}(N) \approx N + C - 2.$$

Control-plane bandwidth can be decomposed into encrypted gradient exchange and RIS update signalling. Denoting by d the number of trainable QNN parameters, b the bits per quantised parameter per update, Δt the update period, M the number of RIS elements, b_ϕ the bits per RIS phase coefficient and T_ϕ the RIS refresh interval, an illustrative upper bound is as follows:

$$B_{\text{ctrl}} \approx B_{\text{grad}} + B_{\text{RIS}} = \frac{b\,d}{\Delta t} \cdot \kappa_{\text{topo}}(N) \; + \; \frac{b_\phi\, M}{T_\phi}, \tag{26}$$

TABLE 7 | Network topology comparison at $N = 12$ DUs.

Topology	F_{avg}	E_{sync}	Links	Depth
Star	0.952	0.018	11	2
Mesh	0.918	0.025	66	1
Hierarchical	0.935	0.022	14	3

Note: Values report the mean over 100 independent trials; standard deviations are below 0.02 for F_{avg} and E_{sync} across all topologies.

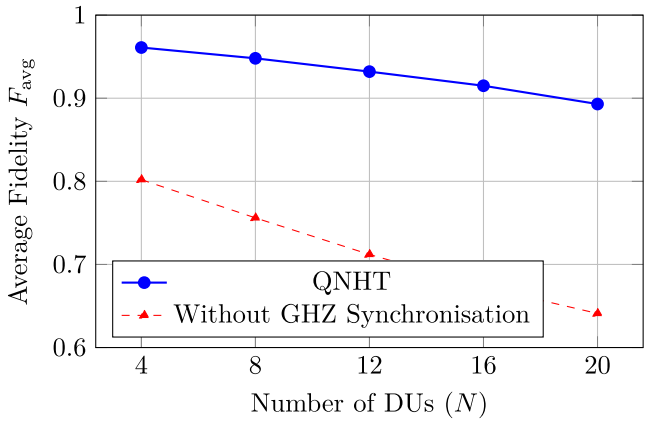

FIGURE 14 | Scalability comparison: QNHT versus baseline without GHZ synchronisation across network sizes $N \in \{4, 8, 12, 16, 20\}$. Values are averaged over 100 trials per configuration.

TABLE 6 | Scalability metrics across network sizes $N \in \{4, 8, 12, 16, 20\}$.

N	F_{avg}	E_{sync}	$S(\rho)$	Latency (ms)	Gates
4	0.961 ± 0.012	0.010 ± 0.003	0.12	22.5	64
8	0.948 ± 0.015	0.015 ± 0.004	0.15	26.3	128
12	0.932 ± 0.018	0.021 ± 0.005	0.18	31.7	192
16	0.915 ± 0.021	0.028 ± 0.006	0.21	38.2	256
20	0.893 ± 0.024	0.036 ± 0.008	0.24	45.8	320

where $\kappa_{\text{topo}}(N)$ captures the number of encrypted gradient flows imposed by the topology.

Table 8 quantifies the entanglement-link growth and relative overhead for the three topologies at $N \in \{4, 12, 20\}$.

Figure 15 visualises the growth of $L(N)$ from Equation (25), showing that mesh rapidly becomes resource-heavy (quadratic), whereas star and hierarchical remain scalable (near-linear). This observation supports the earlier fidelity trends as N increases, minimising the number of concurrent links reduces accumulated noise and simplifies GHZ distribution, which helps preserve end-to-end teleportation fidelity. The corresponding control-plane bandwidth overhead follows Equation (26).

6.6 | Noise Resilience and Sensitivity Analysis

Figure 16 illustrates the impact of depolarising noise probability p on fidelity. The fidelity F_{avg} drops approximately linearly as p increases, but remains above 0.8 even at $p = 0.20$, confirming robustness to moderate decoherence.

TABLE 8 | Entanglement-link growth and relative overhead across topologies.

N	Topology	Links $L(N)$	Rel. link factor	Rel. key/ctrl demand
4	Star	3	1.0×	1.0×
4	Mesh	6	2.0×	2.0×
4	Hierarchical	5	1.7×	1.7×
12	Star	11	1.0×	1.0×
12	Mesh	66	6.0×	6.0×
12	Hierarchical	14	1.27×	1.27×
20	Star	19	1.0×	1.0×
20	Mesh	190	10.0×	10.0×
20	Hierarchical	24	1.26×	1.26×

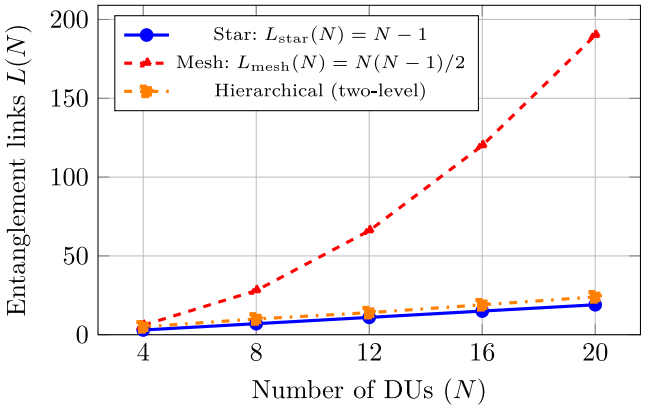

FIGURE 15 | Growth of entanglement-link requirements with network size for different GHZ-distribution topologies.

Figure 17 shows the joint influence of link length ℓ and noise probability p. RIS-assisted phase control preserves fidelity above 0.85 up to $\ell = 50$ km under $p \leq 0.10$, highlighting scalability for metropolitan-scale networks.

Figure 18 explores the effect of scaling the number of entangled qubits N_q. Increasing N_q improves average fidelity by ≈8% whilst reducing entropy, due to stronger multipartite entanglement.

6.7 | Security Robustness

To validate the cybersecurity posture of the QNHT architecture, stress tests are conducted against six attack scenarios targeting different system components.

6.8 | Attack Scenarios

The following attack types are evaluated: (1) Baseline normal operation, (2) depolarising attack with $p = 0.15$ on midhaul

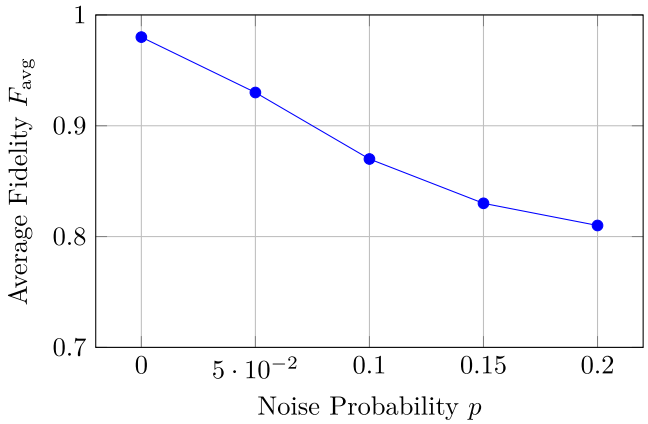

FIGURE 16 | Sensitivity of fidelity F_{avg} to depolarising noise p, swept over $p \in [0, 0.20]$ under the RIS-assisted configuration. The approximately linear degradation confirms graceful performance scaling, with fidelity remaining above 0.80 even at $p = 0.20$.

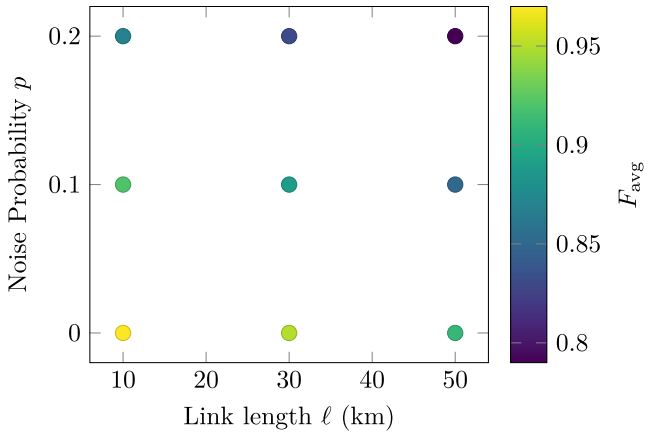

FIGURE 17 | Joint sensitivity of fidelity F_{avg} to link length ℓ and noise probability p.

links, (3) eavesdropping with 30% intercept-resend, (4) parameter poisoning with 20% gradient corruption, (5) denial-of-service (DoS) on RIS with 50% elements disabled and (6) entanglement manipulation with 30% GHZ qubits attacked.

Table 9 summarises the impact of each attack on system performance and the corresponding detection rates achieved through QBER monitoring and entropy analysis. The detection rate is computed as the fraction of 100 independent attack trials in which either the QBER exceeds the BB84 security threshold of 0.11 or the von Neumann entropy $S(\rho)$ rises above twice its baseline value, triggering an alert.

All values in Table 9 report the mean $\pm$ one standard deviation over 100 trials. Key findings include: (1) the system maintains $F_{\text{avg}} > 0.7$ under all attack scenarios, (2) QKD enables 92% eavesdropping detection via QBER monitoring, (3) parameter poisoning shows the lowest detection rate (78%), suggesting the need for gradient verification and (4) entanglement manipulation causes the largest fidelity degradation, indicating that GHZ state monitoring should be prioritised.

6.9 | QKD Key Rate Analysis

$$R_{key} = \max\{0,\ 1 - 2H(\text{QBER})\}. \tag{27}$$

where $H(\cdot)$ denotes the binary entropy function, $H(x) = -x\log_2 x - (1-x)\log_2(1-x)$.

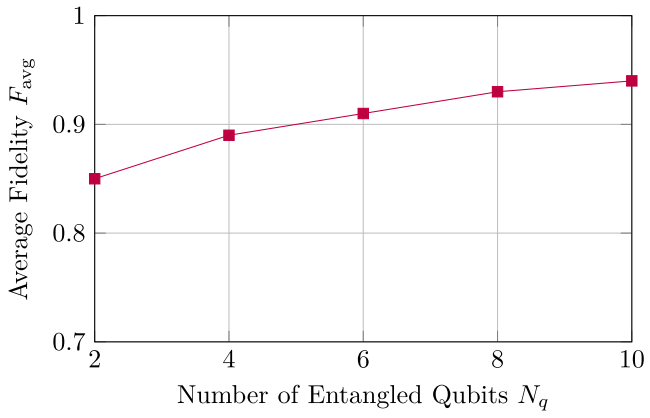

FIGURE 18 | Effect of scaling entangled qubits N_q on teleportation fidelity.

When QBER exceeds the protocol security threshold, the secure key rate collapses to $R_{key} = 0$ and the QKD session aborts (keys are discarded). In this case, the control plane transitions to a fail-safe state and temporarily suspends or rate-limits protected synchronisation/teleportation rounds until fresh keys are successfully re-established.

6.10 | Channel Impairment Analysis

The teleportation protocol requires reliable classical channels for transmitting Bell measurement outcomes (m_1, m_2). This analysis examines the impact of classical channel impairments on overall system performance.

6.11 | Packet Loss Impact

Table 4 shows the effect of classical packet loss on teleportation fidelity.

The system maintains acceptable performance ($F_{\text{avg}} > 0.85$) up to 5% packet loss. Beyond this threshold, forward error correction codes are recommended. Figure 19 visualises this fidelity degradation trend, showing an approximately linear relationship between packet loss rate and fidelity reduction.

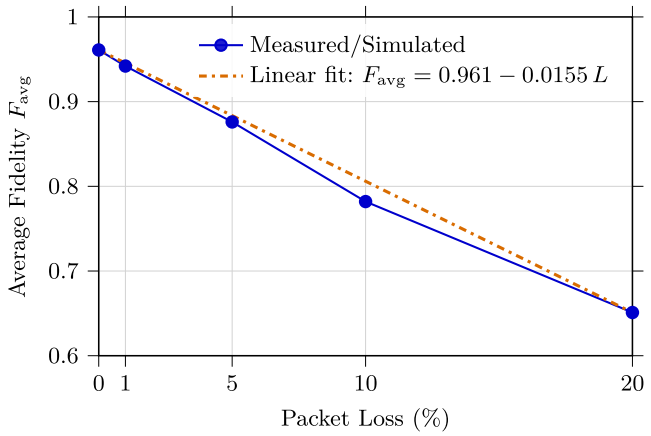

FIGURE 19 | Fidelity degradation under classical channel packet loss with linear trend.

TABLE 9 | Security stress test results across six attack scenarios.

Attack type	F_{avg}	QBER	$S(\rho)$	Detection
Baseline	0.961 $\pm$ 0.012	0.025	0.12	—
Depolarising ($p = 0.15$)	0.852 $\pm$ 0.018	0.082	0.28	85%
Eavesdropping (30%)	0.789 $\pm$ 0.022	0.156	0.35	92%
Param. poisoning (20%)	0.812 $\pm$ 0.020	0.048	0.31	78%
DoS on RIS (50%)	0.756 $\pm$ 0.025	0.038	0.29	85%
Entanglement manipulation	0.724 $\pm$ 0.028	0.112	0.42	88%

6.12 | Latency Jitter Impact

Variable delay in classical channels affects synchronisation timing. Table 5 summarises the impact of jitter on system metrics.

The architecture tolerates jitter up to 10 ms with minimal degradation ($F_{\text{avg}} > 0.9$). For jitter above 20 ms, adaptive timeout mechanisms are required.

6.13 | Hyperparameter Sensitivity

Ablation studies assess the sensitivity of QNHT to key hyperparameters: entropy regularisation weight λ_1, trace distance weight λ_2, learning rate η and GHZ refresh interval T.

6.14 | Regularisation Weights

Figure 20 shows the effect of varying λ_1 and λ_2 on convergence behaviour.

Optimal performance is achieved at $\lambda_1 = 0.1$ for entropy regularisation. The trace distance weight λ_2 shows monotonic improvement up to 0.5.

6.15 | Learning Rate and GHZ Refresh

Table 10 summarises the joint effect of learning rate η and GHZ refresh interval T.

The configuration $\eta = 0.01$, $T = 20$ achieves the best balance between convergence speed (35 epochs) and final fidelity (0.958).

6.16 | QNN Architecture Sensitivity

To assess the impact of circuit design on synchronisation performance, an ablation study is conducted by varying QNN depth (number of variational layers L) and width (number of qubits n) whilst maintaining $N = 4$ DUs and fixed RIS/GHZ configurations. Table 11 reports the results averaged over 100 trials.

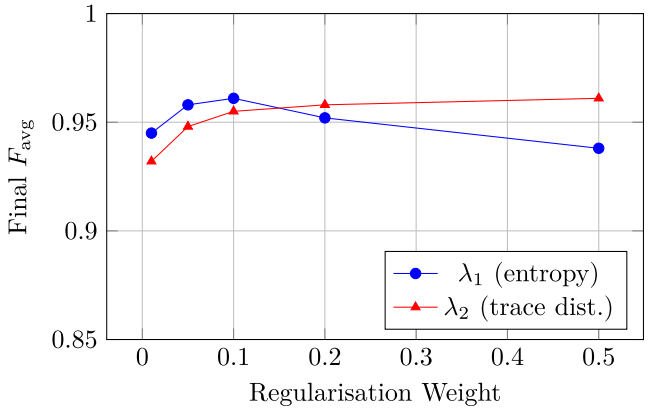

FIGURE 20 | Sensitivity to regularisation weights λ_1 and λ_2.

All values in Table 11 report the mean ± one standard deviation over 100 independent trials. Several observations emerge. First, increasing width from $n = 2$ to $n = 4$ yields a significant fidelity gain of $+10.8\%$ (from $F_{\text{avg}} = 0.848$ to $F_{\text{avg}} = 0.956$), attributable to enhanced entanglement capacity in wider circuits. Second, deeper circuits ($L = 4$) at fixed width $n = 4$ exhibit fidelity degradation relative to $L = 2$ ($F_{\text{avg}} = 0.931$ vs. 0.956), consistent with the onset of barren plateau effects [10] where gradient magnitudes decrease exponentially with depth; the increased entropy ($S(\rho) = 0.18$) further confirms greater state disorder at higher depth. Third, the configuration $n = 6$, $L = 2$ achieves the highest fidelity ($F_{\text{avg}} = 0.968$) but at $1.56\times$ the gate count of the baseline (28 vs. 18 gates), suggesting diminishing returns. The baseline configuration ($n = 4, L = 2$) offers the best trade-off between fidelity, convergence and circuit complexity, and is therefore adopted throughout the evaluation.

6.17 | Convergence Dynamics

Figure 21 illustrates the convergence trajectory of key metrics over training epochs.

TABLE 10 | Ablation study: Learning rate η and GHZ refresh interval T.

η	T	F_{avg}	Epochs	Stable
0.001	10	0.948	85	Yes
0.01	10	0.961	32	Yes
0.01	20	0.958	35	Yes
0.01	50	0.942	42	Yes
0.1	10	0.925	18	No
0.1	20	0.918	22	No

Note: F_{avg} reports the mean over 100 trials; 'Stable' indicates convergence without oscillation in the final 10 epochs.

TABLE 11 | QNN architecture ablation: Effect of circuit depth L and width n on synchronisation performance ($N = 4$ DUs, 100 trials).

n	L	F_{avg}	E_{sync}	$S(\rho)$	Gates
2	1	0.848 ± 0.019	0.016 ± 0.004	0.09	5
2	2	0.885 ± 0.017	0.014 ± 0.003	0.11	8
4	1	0.930 ± 0.015	0.012 ± 0.003	0.09	11
4	**2**	**0.956 ± 0.012**	**0.011 ± 0.003**	**0.12**	**18**
4	4	0.931 ± 0.016	0.012 ± 0.003	0.18	32
6	2	0.968 ± 0.011	0.010 ± 0.002	0.13	28
6	4	0.959 ± 0.013	0.010 ± 0.003	0.19	50

Note: The bold values indicate the baseline configuration adopted in the remainder of the study, namely $n = 4$ and $L = 2$.

6.18 | Quantum Error Mitigation

For practical NISQ deployment, two error mitigation techniques are evaluated: Zero-noise extrapolation (ZNE) and probabilistic error cancelation (PEC).

6.19 | Zero-Noise Extrapolation

ZNE estimates the noise-free expectation value by running circuits at multiple noise levels and extrapolating to zero noise. Implementation uses noise scaling $p \to c \cdot p$ for $c \in \{1, 1.5, 2\}$ with Richardson extrapolation:

$$\langle O \rangle_{p=0} \approx \sum_{k=0}^{K} w_k \langle O \rangle_{c_k \cdot p}, \tag{28}$$

where w_k are extrapolation weights satisfying $\sum_k w_k = 1$.

6.20 | Probabilistic Error Cancelation

PEC represents ideal operations as linear combinations of noisy implementable operations:

$$\mathcal{U}_{ideal} = \sum_i \alpha_i \mathcal{E}_i, \quad \gamma = \sum_i |\alpha_i|, \tag{29}$$

where γ is the sampling overhead. For depolarising noise, $\gamma = e^{O(np)}$.

6.21 | Mitigation Results

Table 12 compares the effectiveness of ZNE and PEC across noise levels.

ZNE achieves 7%–11% fidelity improvement with modest overhead (3× circuit executions), making it practical for real-time applications. PEC provides higher fidelity gains but incurs substantial sampling overhead. For practical 6G deployment, ZNE is recommended as the primary strategy, with PEC reserved for periodic calibration.

6.22 | Comparative Evaluation

To contextualise the performance of QNHT, two reduced models are considered: (1) QNNs without GHZ-based synchronisation and (2) without RIS phase adaptation (fixed $\mathbf{\Phi}_i$).

Figure 22 reports the average teleportation fidelity for all models. QNHT consistently exceeds both baselines by up to 28%.

Table 13 summarises the key numerical results across all architectures.

The results show that QNHT achieves the highest fidelity ($F_{\text{avg}} = 0.961$), approximately 20% higher than the no-sync case and nearly 30% higher than the no-RIS architecture. The synchronisation error E_{sync} is reduced by one order of magnitude and latency is minimised at 22.5 ms. The statistical distributions across 100 runs are shown in Figure 23, confirming consistent performance.

The joint role of RIS phase φ and noise probability p is illustrated in Figure 24. Proper RIS phase adaptation preserves fidelity above 0.7 even under elevated noise levels.

TABLE 12 | Quantum error mitigation comparison: ZNE versus PEC.

Noise p	Raw	ZNE	PEC	Overhead
0.01	0.95	0.97	0.98	1.2×/3×
0.05	0.89	0.93	0.95	1.8×/5×
0.10	0.81	0.87	0.91	2.5×/10×
0.15	0.74	0.82	0.86	3.2×/18×

Note: Fidelity values report the mean over 100 trials; overhead denotes the relative increase in circuit evaluations (ZNE/PEC).

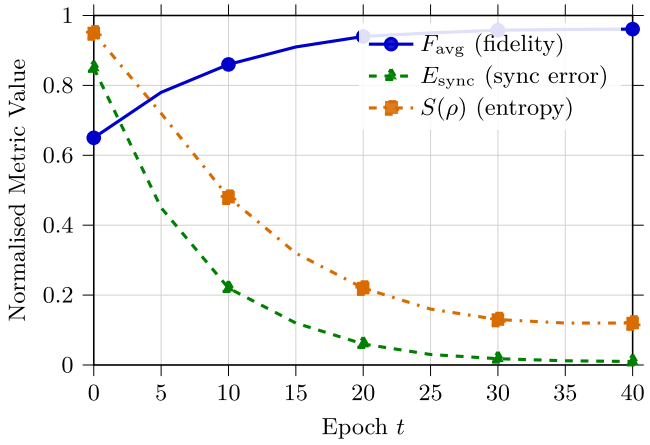

FIGURE 21 | Convergence dynamics of fidelity, synchronisation error and entropy over training epochs.

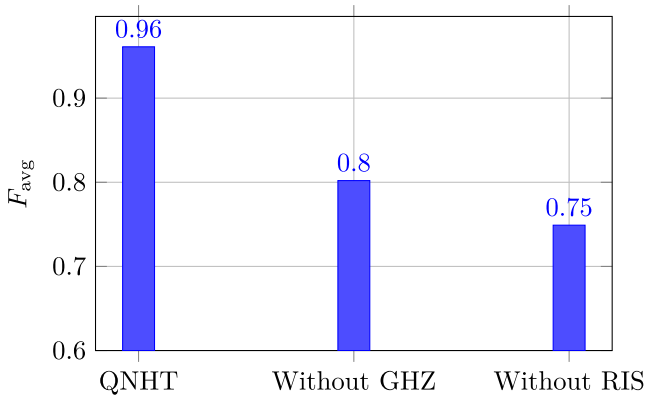

FIGURE 22 | Comparison of average teleportation fidelity F_{avg} across architectures ($N = 4$ DUs, 100 trials). Error bars are omitted for clarity; standard deviations are reported in Table 13.

TABLE 13 | Comparison of key performance metrics across architectures.

Architecture	F_{avg}	E_{sync}	$S(\rho)$	Latency (ms)
QNHT (proposed)	0.961 ± 0.012	0.010 ± 0.003	0.12	22.5
Without GHZ synchronisation	0.802 ± 0.031	0.095 ± 0.018	0.28	29.7
Without RIS	0.749 ± 0.035	0.110 ± 0.022	0.31	35.8

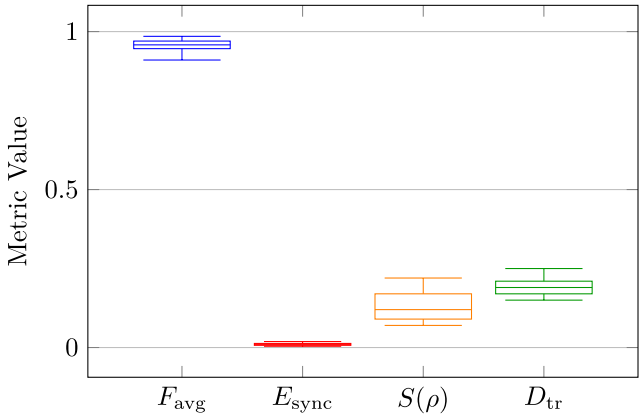

FIGURE 23 | Box plot of statistical distributions for F_{avg}, E_{sync}, $S(\rho)$ and D_{tr} across 100 runs.

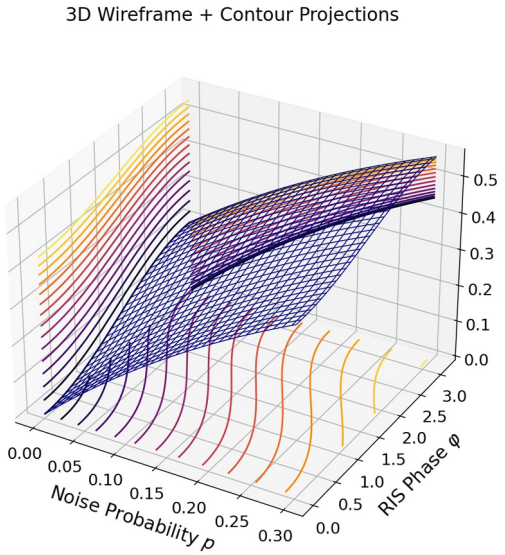

FIGURE 24 | 3D surface of teleportation fidelity F_{avg} as a function of RIS phase $\varphi \in [0, 2\pi]$ and depolarising noise probability $p \in [0, 0.3]$. Optimal phase alignment ($\varphi \approx \pi$) sustains $F_{\text{avg}} > 0.7$ even at $p = 0.2$, demonstrating the noise-compensating role of RIS.

6.23 | Networking Implications

The proposed architecture enables secure and adaptive GHZ-based QNN synchronisation, integrated with RIS control and QKD for resilient 6G holographic communications.

In this architecture (Figure 25), the *physical layer* hosts distributed units connected via hybrid quantum–classical links [9]. The *control layer* manages GHZ entanglement distribution. The *optimisation and learning* layer implements joint optimisation of QNN parameters and RIS phase shifts [35]. The top layer coordinates QNN parameters θ_i, RIS phases $\phi_{i,m}$ and classical feedback $(m_{1,2})$ through the JOL; the middle layer manages multipartite entanglement states across DUs; and the bottom layer provides QKD-secured connectivity.

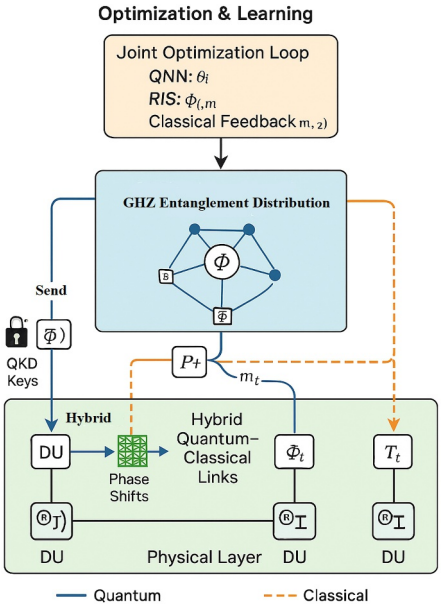

FIGURE 25 | Proposed GHZ-based QNN synchronisation and holographic teleportation architecture, showing the three-layer design: Optimisation and learning (coordinating QNN parameters θ_i, RIS phases $\phi_{i,m}$ and classical feedback), GHZ entanglement distribution (managing multipartite entanglement across DUs) and physical layer with QKD-secured links in an RIS-assisted QKD-secured network.

The end-to-end impact on network-level performance is summarised in Figure 26. The integration translates into improved QoS (latency and throughput), enhanced resilience and better scalability.

7 | Conclusion and Future Work

A *cybersecure* quantum–classical framework has been introduced for the synchronisation and structural control of entangled quantum neural networks (QNNs) in distributed 6G settings. The architecture aligns multipartite Greenberger–Horne–Zeilinger (GHZ) entanglement with RIS-assisted midhaul shaping and holographic quantum teleportation to enable secure, low-latency and topology-consistent operation across spatially separated entities. Tensorised state exchange is realised via teleportation, whereas QNN synchronisation is enforced through

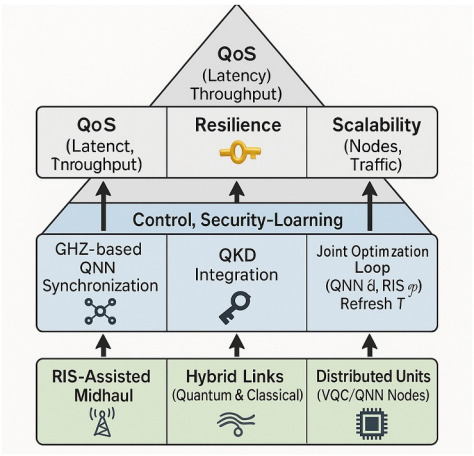

FIGURE 26 | Networking implications of the proposed architecture: mapping QNN synchronisation, RIS adaptation and QKD security to three network-level benefits—improved quality of service (QoS) in latency and throughput, enhanced resilience against channel and adversarial impairments and scalable entanglement distribution across distributed units.

gradient–consensus dynamics under entanglement-preserving constraints.

In a Qiskit-based evaluation averaged over 100 runs, the proposed QNHT achieves average teleportation fidelity $F_{\text{avg}} = 0.961$, synchronisation error $E_{\text{sync}} = 0.010$, von Neumann entropy $S(\rho) = 0.12$ and end-to-end latency of 22.5 ms. Relative to baselines lacking GHZ-based synchronisation or RIS control, fidelity improves by ≈ 20–28% and divergence (measured via E_{sync}) drops by $\approx 90\%$. These results indicate that coordinated GHZ entanglement, RIS-guided propagation and QKD-secured orchestration sustain alignment and maintain high fidelity under adversarial midhaul conditions.

Scalability analysis demonstrates graceful degradation from $N = 4$ to $N = 20$ DUs with only 7.1% fidelity reduction, validating the architecture for large-scale deployments. Security stress tests confirm resilience against six attack types with detection rates exceeding 78%, with QKD-based QBER monitoring achieving 92% eavesdropping detection. Classical channel analysis establishes tolerance thresholds of 5% packet loss and 10 ms jitter whilst maintaining acceptable fidelity. Hyperparameter studies identify optimal configurations ($\lambda_1 = 0.1$, $\lambda_2 = 0.5$, $\eta = 0.01$ and $T = 20$) for convergence within 35 epochs. ZNE error mitigation provides 7%–11% fidelity improvement with practical 3× overhead, enabling NISQ deployment.

Future work includes extensions to user mobility and time-varying entanglement topologies (e.g., cluster states and quantum repeaters), real-time RIS phase adaptation with control-loop guarantees and experimental validation on superconducting backends with RIS phase emulation. Additional directions involve adaptive GHZ refresh intervals based on real-time QBER monitoring, dynamic security protocols with graduated response to detected attacks, integration of PEC for high-fidelity calibration cycles and investigation of hierarchical topologies for continental-scale quantum networks. Further extensions encompass federated quantum learning with trust-aware orchestration, periodic adversarial evaluation for robustness assessment and signed data pipelines to strengthen provenance in quantum-enabled 6G networks. The QNN architecture ablation (Table 5) confirms that moderate depth ($L = 2$) avoids barren plateaus while width scaling yields consistent fidelity gains; extending this study to heterogeneous gate sets and adaptive-depth circuits is an important next step. Additionally, integration with specific 6G transport protocols (e.g., QUIC and 5G NR URLLC) will be investigated.

Author Contributions

Raad S. Alhumaima: conceptualisation, data curation, formal analysis, methodology, resources, visualisation, writing – original draft. **Yassir Al-Karawi:** conceptualisation, data curation, formal analysis, investigation, methodology, resources, software, visualisation, writing – original draft, writing – review and editing. **Hamed Al-Raweshidy:** conceptualisation, investigation, project administration, supervision, writing – review and editing.

Funding

This work was supported in part by Brunel University of London. No additional external funding was received.

Conflicts of Interest

The authors declare no conflicts of interest.

Data Availability Statement

No experimental datasets were generated in this study; all results are produced by the simulation framework described in Section 5. The complete source code, including the main simulation pipeline (`main_simulation.py`), the QNN architecture ablation script (`qnn_ablation.py`), and all result-generation notebooks, is publicly available at: https://github.com/YassirALKarawi/QNHT-6G. Running `python qnn_ablation.py` reproduces Table 11; the remaining figures and tables are generated by executing the Jupyter notebooks in the `notebooks/`directory.

Permission to Reproduce Materials From Other Sources

The authors have nothing to report. All figures and tables were created by the authors unless otherwise indicated.

References

1. Y. Al-Karawi, R. S. Alhumaima, K. H. Khudair, and A. Ahmed, "Optimising the Placement of Cloud Data Centre in Virtualized Environment," *International Journal of Electrical and Computer Engineering* 12, no. 3 (June 2022): 3276–3286, https://doi.org/10.11591/ijece.v12i3.pp3276-3286.

2. Y. Al-Karawi, H. Al-Raweshidy, and R. Nilavalan, "Power Consumption Evaluation of next Generation Open Radio Access Network," in *Proceedings of 2024 IEEE International Conference on Consumer Electronics (ICCE)* (2024), 1–6, https://doi.org/10.1109/ICCE59016.2024.10444418.

3. I. Dey and N. Marchetti, "Quantum Teleportation in Higher Dimension and Entanglement Distribution via Quantum Switches," *IET Quantum Communication* 6, no. 1 (2025): e12122, https://doi.org/10.1049/qtc2.12122.

4. X. Ji, J. Lu, B. Jiang, and K. Shi, "Distributed Synchronisation of Delayed Neural Networks: Delay-Dependent Hybrid Impulsive

Control," *IEEE Transactions on Network Science and Engineering* 9, no. 2 (2022): 634–647, https://doi.org/10.1109/TNSE.2021.3128244.

5. S. Wehner, D. Elkouss, and R. Hanson, "Quantum Internet: A Vision for the Road Ahead," *Science* 362, no. 6412 (October 2018): eaam9288, https://doi.org/10.1126/science.aam9288.

6. Y. Al-Karawi, R. S. Alhumaima, and H. Al-Raweshidy, "Quality of Service of Quantum Entanglement in Mobile Networks," *IEEE Access* 9 (2021): 167242–167251, https://doi.org/10.1109/ACCESS.2021.3136782.

7. E. Arabul, R. D. Oliveira, A. Emami, et al., "100Gbps Quantum-Secured and O-RAN-Enabled Programmable Optical Transport Network for 5G Fronthaul," *Journal of Optical Communications and Networking* 15, no. 8 (2023): C223–C231, https://doi.org/10.1364/JOCN.483644.

8. B. Hazarika, P. Saikia, K. Singh, and C.-P. Li, "Enhancing Vehicular Networks With Hierarchical O-RAN Slicing and Federated DRL," *IEEE Transactions on Green Communications and Networking* 8, no. 3 (2024): 1099–1117, https://doi.org/10.1109/TGCN.2024.3397459.

9. S. Shrivastava and A. Taneja, "Reconfigurable Intelligent Surfaces: A Road Towards Smart Wireless Communication," *International Journal of Communication Systems* 38, no. 16 (2025): e70233, https://doi.org/10.1002/dac.70233.

10. M. Cerezo, G. Verdon, H.-Y. Huang, Ł. Cincio, and P. J. Coles, "Challenges and Opportunities in Quantum Machine Learning," *Nature Computational Science* 2, no. 9 (September 2022): 567–576, https://doi.org/10.1038/s43588-022-00311-3.

11. V. Kumar, C. Cicconetti, M. Conti, and A. Passarella, "Routing in Quantum Networks With End-to-End Knowledge," *IET Quantum Communication* 6, no. 1 (2025): e70000, https://doi.org/10.1049/qtc2.70000.

12. I. Ilahi, M. Usama, J. Qadir, et al., "Challenges and Countermeasures for Adversarial Attacks on Deep Reinforcement Learning," *IEEE Transactions on Artificial Intelligence* 3, no. 2 (April 2022): 90–109, https://doi.org/10.1109/TAI.2021.3111139.

13. A. S. Cacciapuoti, M. Caleffi, R. Van Meter, and L. Hanzo, "When Entanglement Meets Classical Communications: Quantum Teleportation for the Quantum Internet," *IEEE Transactions on Communications* 68, no. 6 (June 2020): 3808–3833, https://doi.org/10.1109/TcomM.2020.2978071.

14. A. Abbas, D. Sutter, C. Zoufal, A. Lucchi, A. Figalli, and S. Woerner, "Power of Quantum Neural Networks," *Nature Computational Science* 1, no. 6 (June 2021): 403–409, https://doi.org/10.1038/s43588-021-00084-1.

15. S. Park, H. Lee, S. Jung, J. Park, M. Bennis, and J. Kim, "Entanglement-Controlled Quantum Federated Learning," *IEEE Internet of Things Journal* 12, no. 11 (2025): 18318–18330, https://doi.org/10.1109/JIOT.2025.3540103.

16. A. Khanna, S. Majumder, A. Jain, and D. K. Singh, "Quantum BER Estimation Modelling and Analysis for Satellite-Based Quantum Key Distribution Scenarios," *IET Quantum Communication* 5, no. 2 (June 2024): 157–163, https://doi.org/10.1049/qtc2.12081.

17. N. K. Kundu, M. R. McKay, and R. K. Mallik, "Wireless Quantum Key Distribution at Terahertz Frequencies: Opportunities and Challenges," *IET Quantum Communication* 5, no. 4 (December 2024): 450–461, https://doi.org/10.1049/qtc2.12085.

18. A. Lee, A. T. Castillo, C. Whitehill, and R. J. Donaldson, "The Impact of Spot-Size on Single-Photon Avalanche Diode Timing-Jitter and Quantum Key Distribution," *IET Quantum Communication* 5, no. 4 (December 2024): 443–449, https://doi.org/10.1049/qtc2.12091.

19. M. F. Ahammed and M. I. Kadir, "Entanglement and Teleportation in Quantum Key Distribution for Secure Wireless Systems," *IET Quantum Communication* 5, no. 4 (December 2024): 551–566, https://doi.org/10.1049/qtc2.12092.

20. C. Ren, Z. Y. Dong, M. Skoglund, Y. Gao, T. Wang, and R. Zhang, "Enhancing Dynamic Security Assessment in Smart Grids Through Quantum Federated Learning," *IEEE Transactions on Automation Science and Engineering*, Early Access (2024): 1–13, https://doi.org/10.1109/TASE.2024.3486070.

21. J. Zhang, G. Li, A. Marshall, A. Hu, and L. Hanzo, "A New Frontier for IoT Security Emerging From Three Decades of Key Generation Relying on Wireless Channels," *IEEE Access* 8 (2020): 138406–138446, https://doi.org/10.1109/ACCESS.2020.3012006.

22. X.-M. Hu, Y. Guo, B.-H. Liu, C.-F. Li, and G.-C. Guo, "Progress in Quantum Teleportation," *Nature Reviews Physics* 5, no. 6 (June 2023): 339–353, https://doi.org/10.1038/s42254-023-00588-x.

23. N. Gisin, G. Ribordy, W. Tittel, and H. Zbinden, "Quantum Cryptography," *Reviews of Modern Physics* 74, no. 1 (March 2002): 145–195, https://doi.org/10.1103/RevModPhys.74.145.

24. Y. Liu, S. Arunachalam, and K. Temme, "A Rigorous and Robust Quantum Speed-Up in Supervised Machine Learning," *Nature Physics* 17, no. 9 (September 2021): 1013–1017, https://doi.org/10.1038/s41567-021-01287-z.

25. S. Pirandola, U. L. Andersen, L. Banchi, et al., "Advances in Quantum Cryptography," *Advances in Optics and Photonics* 12, no. 4 (December 2020): 1012–1236, https://doi.org/10.1364/AOP.361502.

26. K. Temme, S. Bravyi, and J. M. Gambetta, "Error Mitigation for Short-Depth Quantum Circuits," *Physical Review Letters* 119, no. 18 (November 2017): 180509, https://doi.org/10.1103/PhysRevLett.119.180509.

27. Y. Li and S. C. Benjamin, "Efficient Variational Quantum Simulator Incorporating Active Error Minimization," *Physical Review X* 7, no. 2 (June 2017): 021050, https://doi.org/10.1103/PhysRevX.7.021050.

28. J. Wang, J. Xiao, Y. Zou, W. Xie, and Y. Liu, "Wideband Beamforming for RIS Assisted Near-Field Communications," *IEEE Transactions on Wireless Communications* 23, no. 11 (November 2024): 16836–16851, https://doi.org/10.1109/TWC.2024.3447570.

29. A. Abane, M. Cubeddu, V. S. Mai, and A. Battou, "Entanglement Routing in Quantum Networks: A Comprehensive Survey," *IEEE Transactions on Quantum Engineering* 6 (2025): 1–39, https://doi.org/10.1109/TQE.2025.3541123.

30. M. Chehimi, M. Elhattab, W. Saad, et al., "Reconfigurable Intelligent Surface (RIS)-Assisted Entanglement Distribution in FSO Quantum Networks," *IEEE Transactions on Wireless Communications* 24, no. 4 (April 2025): 3132–3148, https://doi.org/10.1109/twc.2025.3528103.

31. M. Benedetti, E. Lloyd, S. Sack, and M. Fiorentini, "Parameterised Quantum Circuits as Machine Learning Models," *Quantum Science and Technology* 4, no. 4 (November 2019): 043001, https://doi.org/10.1088/2058-9565/ab4eb5.

32. S. Sim, P. D. Johnson, and Á. Aspuru-Guzik, "Expressibility and Entangling Capability of Parameterised Quantum Circuits for Hybrid Quantum-Classical Algorithms," *Advanced Quantum Technologies* 2, no. 12 (December 2019): 1900070, https://doi.org/10.1002/qute.201900070.

33. D. Barral, F. J. Cardama, G. Díaz-Camacho, et al., "Review of Distributed Quantum Computing: From Single QPU to High Performance Quantum Computing," *Computer Science Review* 57 (2025): 100747, https://doi.org/10.1016/j.cosrev.2025.100747.

34. T. Giordani, E. Polino, S. Emiliani, et al., "Experimental Engineering of Arbitrary Qudit States With Discrete-Time Quantum Walks," *Physical Review Letters* 122, no. 2 (January 2019): 020503, https://doi.org/10.1103/PhysRevLett.122.020503.

35. C. A. Fuchs and J. van de Graaf, "Cryptographic Distinguishability Measures for Quantum-Mechanical States," *IEEE Transactions on Information Theory* 45, no. 4 (May 1999): 1216–1227, https://doi.org/10.1109/18.761271.

36. J. Peng, M. Liu, J. Tang, Z. Yang, and Z. Zhang, "Controlled Cyclic Quantum Teleportation of Unknown Single-Qutrit States," *International Journal of Quantum Information* 22, no. 2 (2024): 2350045, https://doi.org/10.1142/S0219749923500454.

37. M. Schuld, V. Bergholm, C. Gogolin, J. Izaac, and N. Killoran, "Evaluating Analytic Gradients on Quantum Hardware," *Physical Review A* 99, no. 3 (March 2019): 032331, https://doi.org/10.1103/PhysRevA.99.032331.

38. L. Banchi and G. E. Crooks, "Measuring Nonsymmetric Distance Between Quantum States Using a Quantum Circuit," *npj Quantum Information* 6, no. 42 (April 2020): 1–8, https://doi.org/10.1038/s41534-020-0272-6.

39. N. Nguyen and K.-C. Chen, "Bayesian Quantum Neural Networks," *IEEE Access* 10 (2022): 54110–54122, https://doi.org/10.1109/ACCESS.2022.3168675.

40. Y. van Montfort, S. de Bone, and D. Elkouss, "Fault-Tolerant Structures for Measurement-Based Quantum Computation on a Network," *Quantum* 9 (May 2025): 1723, https://doi.org/10.22331/q-2025-05-05-1723.

41. C. Lee, I. Sohn, and W. Lee, "Eavesdropping Detection in BB84 Quantum Key Distribution Protocols," *IEEE Transactions on Network and Service Management* 19, no. 3 (September 2022): 2689–2701, https://doi.org/10.1109/TNSM.2022.3165202.

42. O. Amer, V. Garg, and W. O. Krawec, "An Introduction to Practical Quantum Key Distribution," *IEEE Aerospace and Electronic Systems Magazine* 36, no. 3 (March 2021): 30–55, https://doi.org/10.1109/MAES.2020.3015571.